THz photoconductivity in light-emitting surface-oxidized Si nanocrystals: the role of large particles

2014 New J. Phys. 16 093013

(http://iopscience.iop.org/1367-2630/16/9/093013)

New Journal of Physics
The open access journal at the forefront of physics
Deutsche Physikalische Gesellschaft DPG | IOP Institute of Physics

THz photoconductivity in light-emitting surface-oxidized Si nanocrystals: the role of large particles

V Zajac[1,3], H Němec[1], C Kadlec[1], K Kůsová[2], I Pelant[2] and P Kužel[1]

[1] Institute of Physics ASCR, Na Slovance 2, 18221 Prague 8, Czech Republic
[2] Institute of Physics ASCR, Cukrovarnická 10, 16253 Prague 6, Czech Republic
[3] Faculty of Mathematics and Physics, Charles University in Prague, Ke Karlovu 3, 12116 Prague 2, Czech Republic
E-mail: kuzelp@fzu.cz

Received 19 February 2014, revised 2 July 2014
Accepted for publication 11 July 2014
Published 12 September 2014

New Journal of Physics **16** (2014) 093013

doi:10.1088/1367-2630/16/9/093013

Abstract

We propose an analytical description of the role of local depolarization fields in the terahertz conductivity of nanostructured samples and demonstrate this approach in a sample composed of silicon nanocrystals. This helps to uncover the nature of charge carrier transport at nanoscale. Time-resolved terahertz conductivity is investigated in an ensemble of silicon nanocrystals fabricated by electrochemical etching of silicon wafer followed by an H_2O_2 oxidizing treatment. The post-etching treatment leads to a decrease in the average nanocrystalline Si core size which enhances luminescence in the visible range. We show that the dominating microscopic photoconductive response of photocarriers is essentially Drude-like owing to the presence of a very small amount of large nanocrystals; the macroscopic character of the response is, however, deeply modified by the depolarization fields. Smaller nanocrystals appreciably contribute to the terahertz conductivity only at high photoexcitation densities where the screening due to depolarization fields suppresses the response of the large particles.

Keywords: ultrafast photoconductivity, Si nanocrystals, charge carrier transport, terahertz spectroscopy

1. Introduction

The electronic and optical properties of semiconductors can be tailored nowadays according to requirements using the relevant materials in the form of nanostructures. In particular, silicon nanocrystals (Si NCs) with a size of several nanometers are of fundamental importance for many prospective applications, including photovoltaic devices [1], fluorescence labeling of live cells, cancer tumors and targeted drug delivery [1, 2], light sources and waveguides for silicon photonics [1–3] and Si NCs-based memories [1–3]. While steady-state radiative [4, 5] and nonradiative [6] recombination of optically or electrically injected electrons and holes in Si NCs has been given a great deal of attention in the last two decades, ultrafast electronic excited state relaxation and charge transport ranks among phenomena that have been insufficiently understood until now.

Focusing on Si NCs with oxidized surfaces, it is generally accepted nowadays that upon photo-creating a hot electron–hole pair, first of all energy relaxation (thermalization) of both free electrons and holes on femtosecond time scale sets in; this may be followed, or even accompanied, by ultrafast luminescence, observable using special optical techniques only [7–9]. This light emission can be exploited for optical amplification by stimulated emission on the sub-picosecond time scale [10]. Subsequently, the localization of photocarriers in surface-related states usually takes place. Radiative recombination of these trapped electrons and holes results in long-lived (10–100 μs) orange-red luminescence radiation [11], which represents the principal luminescence feature of Si NCs, denoted as the S(slow)-band.

Of no less importance is the issue of exchanging elementary excitations in large ensembles of closely spaced Si NCs, where they may even be 'in touch' with each other [12]. This can be regarded as an important effect underlying the photoconductivity and/or charge separation in photovoltaic applications of Si NCs. A long-lasting fundamental question of a relation between the charge confinement and the medium- and long-range transport in nanoscaled materials is still awaiting a detailed answer. On the one hand, spectral shifts and characteristic fingerprints in the optical absorption or luminescence spectra indicate a confinement of charge carrier wave functions in NCs; on the other hand, a long range charge transport is clearly observed by classical conductivity measurements and used in various electronic devices such as Grätzel cells [13].

Time-resolved terahertz (THz) spectroscopy appears a very suitable tool to study the initial photocarrier intra- and inter-NC travel without side effects of electrical contacts. Indeed, the probing length of this method, driven basically by the carrier diffusion constant and by the time period of the terahertz wave, is typically of the order of units to tens of nanometers. At the same time, the picosecond length of the terahertz pulses allows one to probe THz photoconductivity spectra at the very initial stage of the carrier transport. By probing relatively large volumes the technique characterizes statistically significant ensembles of nanostructures [14].

Various Si NC films embedded in a SiO_x matrix were previously studied by optical pump–THz probe experiments and the interpretation of the results was based on the phenomenological Drude–Smith model [15–17]. Analysis of time-resolved THz spectra on a microscopic level going beyond phenomenological models is still a challenging task in the case of any NC samples [18, 19]. On top of that, more or less broad distribution of the NC sizes usually exists in real samples and, in many cases, these NCs may be connected by rather complex conductive percolation pathways. In our opinion, the truly microscopic interpretation should explicitly deal with two phenomena [20]: (1) the interaction of mobile carriers with NC

borders [21] and the formation of excitons due to carrier confinement (the strength of these interactions depends on the NC size) and (2) the existence of depolarization fields which screen the incident THz field (these effects depend on the sample morphology and percolation [19, 22]). Both these phenomena lead to the deviation of the measured response from the Drude-like behavior; however, simple fitting of the data e.g. by the phenomenological Drude–Smith model [23] cannot distinguish between their roles in the estimated 'degree' of carrier localization and its origin then remains hidden [24].

In this paper we study carrier transport on a picosecond time scale in silicon NC powder as a function of photoexcitation intensity and as a function of temperature. We develop a method which allows one to distinguish and retrieve the static part (depolarization fields) and dynamical part (microscopic mobility) of the response from the measured THz spectra for both optically thin and thick inhomogeneous samples. The measurements versus photoexcitation density allow us to determine, namely, the sample morphology through the influence of depolarization fields while the temperature dependence provides further hints on the character of the carrier transport at nanoscale.

The paper is organized as follows. In part 2, we recall the relation between the transient THz signal and charge carrier microscopic mobility in inhomogeneous thin films. In part 3, we provide details on sample preparation and characterization and on the THz spectroscopic technique. In part 4, we present the results and discuss them. First we develop a theoretical framework describing the THz signal in optically thick inhomogeneous samples (section 4(A)). Subsequently, in section 4(B), we carry out a qualitative discussion of the measured spectra. Finally, in section 4(C) we propose models of the charge transport and discuss in detail the results of fitting and their relation to the distribution of NC sizes obtained by AFM.

2. Terahertz conductivity in inhomogeneous systems

It is well-known that the optical pump–terahertz (THz) probe experiments can access the response of delocalized or weakly bound charge carriers in photoexcited semiconductors. Usually, the aim is to determine a single-carrier response function represented by the spectrum of microscopic mobility $\mu(\omega)$. However, since the THz radiation probes a macroscopic volume of a (possibly inhomogeneous) sample, the relation between the measured photoconductivity spectrum and the microscopic mobility may be nontrivial.

In the case of a homogeneous bulk semiconductor the microscopic response of carriers is usually band-like, i.e., it is described either directly by the Drude formula or by some of its modifications due to the scattering time distribution [25, 26]. In all these cases the real part of the conductivity decreases with increasing frequency and the imaginary part is positive and exhibits a maximum. Nanoscaled materials are inherently inhomogeneous and the macroscopic response (photoconductivity) usually significantly differs from the above described case [20]. The reason for this behavior can be twofold:

(1) The microscopic mobility spectrum $\mu(\omega)$ of individual charge carriers may show a significant deviation from the Drude-like behavior in the THz spectral range due to their interactions with nanocrystal boundaries [21].

(2) The macroscopic photoconductivity reflects an effective response of charge carriers to an external (THz) electric field and the transformation between the photoconductivity and the microscopic mobility is nonlinear. As a consequence, the spectral shape of the measured

conductivity $\Delta\sigma(\omega)$ differs from that of the microscopic mobility $\mu(\omega)$ [22]. In particular, THz spectra of carriers in *non-percolated* inclusions which are incorporated in an insulating or weakly conducting matrix show a plasmon resonance due to local depolarization fields [27]. In this regime the effective conductive response in the THz spectral range of a macroscopic sample saturates above a certain density of charge carriers. In contrast, the effective THz response of carriers in a *percolated* component scales linearly with charge carrier density (as long as carrier–carrier interaction is negligible and the percolation path is not too complex) [22].

The THz signal transmitted through a photoexcited sample depends on the response of all excited carriers within the sample thickness (along the z-axis). Let us assume that the sample is excited with a pump pulse with the photon fluence ϕ creating an excitation density $N_{\mathrm{exc}} = \phi\alpha$, where α is the effective absorption coefficient of the inhomogeneous sample. The incident fluence ϕ and the excitation densities are extremely important experimental parameters which determine the strength of depolarization fields. Due to the above mentioned nonlinearities, it is convenient to characterize the measured effective response of the inhomogeneous photoexcited sample by transient sheet conductivity [22, 28]:

$$\Delta\Sigma(\omega) = \int_0^L \Delta\sigma(\omega; z)\mathrm{d}z. \tag{1}$$

In [22], the so called normalized transient sheet conductivity X_σ was introduced:

$$X_\sigma(\omega) = \frac{\Delta\Sigma(\omega)}{e\phi} = \frac{\alpha}{eN_{exc}}\Delta\Sigma(\omega) \tag{2}$$

where e is the elementary charge, L is the sample thickness, and $\Delta\sigma(z)$ is the macroscopic in-plane conductivity at a given depth z below the photoexcited sample surface. It has been shown [22, 24] that the macroscopic conductivity can be written as:

$$\begin{aligned}\Delta\sigma(z;\omega) &= V\Delta\sigma_{\mathrm{mic}}(z;\omega) + B\frac{\Delta\sigma_{\mathrm{mic}}(z;\omega)}{1+\varphi\Delta\sigma_{\mathrm{mic}}(z;\omega)} \\ &\equiv \Delta\sigma_P(z;\omega) + \Delta\sigma_{NP}(z;\omega)\end{aligned} \tag{3}$$

with[4]

$$\varphi = \frac{D}{\mathrm{i}\omega\varepsilon_0}.$$

The microscopic (local) conductivity of photoexcited parts of the sample was denoted as $\Delta\sigma_{\mathrm{mic}}$ and ε_0 stands for the vacuum permittivity. The coefficients V, B, and D are determined by the effective medium model of the sample structure and they depend only on the geometry of the percolated and non-percolated parts (i.e. they do not depend on temperature, frequency and excitation density). The first right-hand side term in (3), which is linear in $\Delta\sigma_{\mathrm{mic}}$, stands for the contribution of the percolated photoconductive part of the sample $\Delta\sigma_P$ and the second right-hand side (nonlinear) term represents the contribution of its non-percolated part $\Delta\sigma_{NP}$ [24]. This expression follows from the Bergman representation of effective medium with a single

[4] Note that in this paper we use the same convention of the Fourier transformation and of the complex quantities as in [31] (i.e., $\varepsilon = \varepsilon' - \mathrm{i}\varepsilon''$) which is complex conjugated to that used in [20, 22, 24].

dominant depolarization factor [24] and it is able to describe a large number of morphologies including complex percolation pathways [22]. Expression (3) with particular values of the morphology parameters V, B, and D directly leads e.g. to the Maxwell–Garnett model, which can be used in the case of sparse well-isolated photoconductive inclusions. The values of V, B, and D are then related to each other by specific expressions which depend on the filling fraction and shape factor of inclusions.

By comparing (3) with equation (13) in [20] we find for the Maxwell–Garnett model:

$$V = 0 \tag{4}$$

$$B = \frac{\varepsilon_m (1 + sK) - \varepsilon_{\text{eff}} (1 - s)}{\varepsilon_m (s + K) + \varepsilon_{\text{b}} (1 - s)}, \tag{5}$$

$$D = \frac{(1 - s)}{\varepsilon_m (s + K) + \varepsilon_{\text{b}} (1 - s)}, \tag{6}$$

where ε_m is the permittivity of the matrix, ε_b is the background (ground-state) permittivity of the photoconductive inclusions, and ε_{eff} is the effective permittivity of the sample in the ground state; s is the volume fraction of the inclusions and K is their shape factor [20]. In this way the percolation is excluded and both coefficients B and D are explicitly related to the volume filling factor of the inclusions.

Generalization of this framework to multiple kinds of non-percolated components with different microsopic responses $\Delta\sigma_{\text{mic},j}$ (e.g. several types of NCs) leads to extensive formulae. Nevertheless, for low filling fractions and for the components' permittivity values which are not close to $-K\varepsilon_m$ (usually purely real and negative) (see appendix A), the contributions of individual non-percolated components j are approximately additive, i.e.,

$$\Delta\sigma_{NP} (\omega; z) = \sum_j B_j \frac{\Delta\sigma_{\text{mic},j} (\omega; z)}{1 + \varphi_j \Delta\sigma_{\text{mic},j} (\omega; z)} \tag{7}$$

where the parameters B_j, D_j and φ_j are defined using (5) and (6) with appropriate volume fractions s_j.

The local conductivities $\Delta\sigma_{\text{mic},j}$ are proportional to the density of carriers and to their microscopic mobility in the inclusions. The carrier density decays inside the sample following the Lambert–Beer extinction law; the local conductivities then read:

$$\Delta\sigma_{\text{mic},j} (\omega; z) = e\xi_j \mu_j (\omega) \frac{\alpha_j}{\alpha} N_{\text{exc}} \exp(-\alpha z), \tag{8}$$

where ξ_j and μ_j, are the quantum yield and the mobility of photo-carriers, respectively, in the jth component. The local absorption coefficients α_j in the jth component may differ from each other in some cases, resulting in different excitation densities in individual components: $N_j = \alpha_j N_{\text{exc}}/\alpha \equiv \phi\alpha_j$ then stands for the excitation density in the jth component at the surface of the sample.

The expressions for the transient sheet conductivity (1) and (2) involve integration over the sample thickness which allows one to take into account the interaction of the THz pulse with all the carriers in the sample and the different impact of the depolarization fields at different depths:

$$\Delta X_{\sigma,j} = \frac{\alpha}{\alpha_j} V \xi_j \mu_j + B \frac{\ln\left(1 + \varphi\, e \xi_j \mu_j N_{\mathrm{exc}} \alpha_j / \alpha\right)}{\varphi\, e N_{\mathrm{exc}}}. \tag{9}$$

It follows that the contribution of the percolated part (first right-hand side term) to the normalized sheet conductivity is carrier density independent. This means that the depolarization fields do not influence the conductivity originating in the percolated parts of the sample (except for a constant multiplication factor given by the percolation strength V). In contrast, the contribution of the non-percolated part (second right-hand side term in (9)) depends on N_{exc} in a well-defined nonlinear manner. This term is proportional to the mobility μ_j for small values of N_{exc} while it vanishes in the strong excitation limit.

It follows from (9) that it is crucial to carry out experiments in a broad range of pump intensities to evaluate the suitable effective medium model (coefficients V, B, and D) and, subsequently, to determine the temperature and frequency dependent response functions μ_j.

3. Experimental

We measured the transient THz conductivity of a powder of silicon NCs prepared by electrochemical etching from a B-doped Si wafer [29]. Previous photoluminescence [29], HRTEM and Raman [30] measurements indicate that most of the crystalline phase is etched down to nanocrystals. The histogram of the NC size distribution measured by atomic force microscopy (AFM) is shown in figure 1(*a*) and it peaks at a diameter of about 2.8 nm, but it clearly has a non-negligible large-size tail. Since many physical phenomena do not scale with a particle's diameter linearly, this tail might play an important role. This is evident from figure 1(*b*), presenting the AFM-measured size distribution recalculated to volumic fraction, where the most frequently encountered size (3 nm) has already only a negligible contribution. Thus, this large-size tail was investigated by dynamic light scattering (Zetasizer Nano S V by Malvern) and, in figure 1(*c*), we plot the number-of-particles weighted distribution function measured by this technique. The results confirm the large-size tail in the range ~50–400 nm. However, since the scattered light intensity for particles with sizes close to 100 nm and less decreases with the sixth power of the particle's diameter, d^6, the possible signal from small NCs is completely screened off by larger particles, producing a false zero signal at small sizes. The large-size tail is made up by very large NCs and/or aggregates, which develop as the crystalline cores oxidize, forming silica shells. It is important to note here that a broad size distribution with a small fraction of NCs with a much larger size is not exclusive to our sample, but can be encountered in many types of nanostructures.

From x-ray photoelectron spectroscopy [9] we estimate that isolated crystalline silicon cores occupy about 5% of the aggregate volume in the Si NC powder, the rest being filled by SiO_2 and SiO_x matrix. The question of possible conductive contact between adjacent NCs and charge transport among them has remained unanswered in previous studies of silicon nanocrystals fabricated by electrochemical etching of Si wafers.

The fabricated NC powder was put, and very gently compressed, in a cuvette made of two 1 mm thick c-cut quartz plates separated by a teflon spacer with a 4 mm diameter circular hole in the centre. In our experiment the hole in the spacer was completely filled with the sample powder providing 220–260 μm thick samples. The cuvette was fixed to a 3 mm aperture to limit the measuring area to the central part of the sample and placed in a cryostat with sapphire

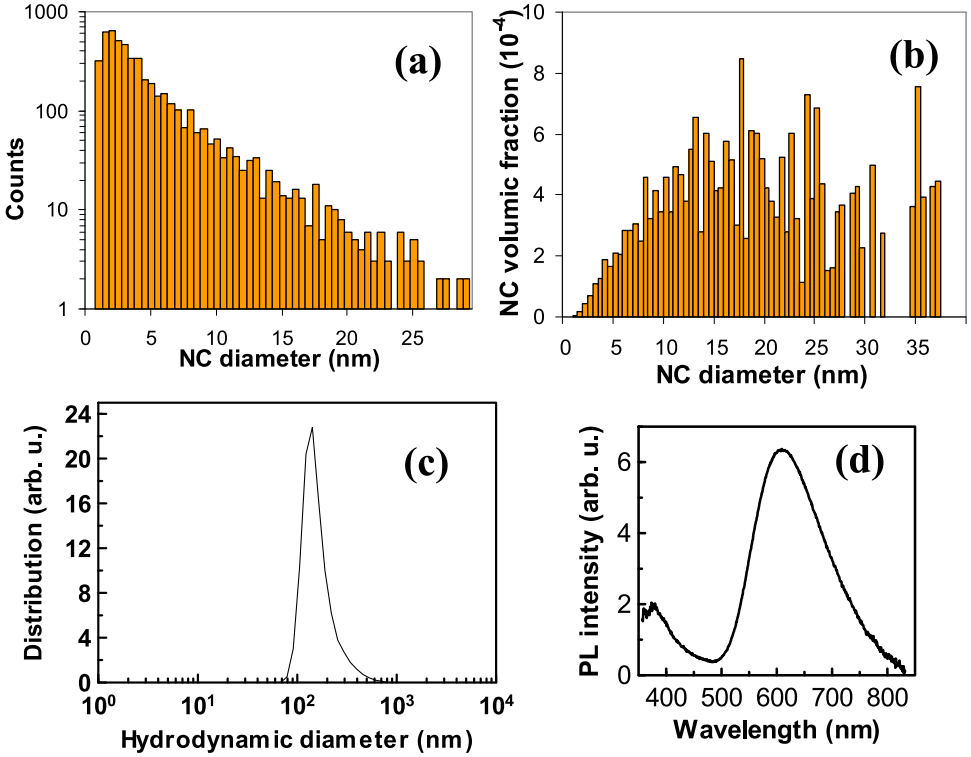

Figure 1. Histograms depicting (*a*) distribution of nanoparticle sizes measured by AFM (after [9], reproduced by permission of The Royal Society of Chemistry); (*b*) distribution of volume fraction of particles in a sample with unit volume (2.5% of Si, 47.5% of SiO_2/SiO_x, 50% of air) calculated from (*a*) assuming spherical particles. Histogram bins: 0.5 nm. Note that AFM cannot distinguish between individual Si NC cores: some larger particles may be composed of smaller NCs. (*c*) Distribution of sizes measured by dynamic light scattering. Note that the measurement is completely insensitive to small particles as the light scattering signal for particles with sizes close to 100 nm or less is proportional to d^6 and thus just a very small fraction of larger particles screens off the signal of small NCs. This makes the dynamic light scattering measurement complimentary to AFM, enabling the study of a large-size tail. (*d*) Photoluminescence spectrum of the sample powder dispersed in ethanol (excitation at 325 nm, 0.6 mW).

windows. Two samples named A and B were prepared from the same dose of etched NC powder; the NC powder for sample A was, in addition, left in a high power ultrasonic bath with ethanol (absorbed energy 400 kJ). This procedure is assumed to split larger agglomerates of NCs into smaller pieces; this could possibly also break narrow conductive channels between NCs if there were any.

The sample used for the AFM measurements in figure 1 was prepared by the same etching procedure, but it underwent a longer ultrasonic treatment in methanol with low concentration of nanocrystals, which led to successful breaking of the agglomerates. This procedure was necessary to enable the measurement of the sizes of nanocrystals; however, this particular sample could not be used for THz measurements due to the low concentration of nanocrystals present.

The measured effective THz refractive index is about 1.45 for sample A and 1.33 for sample B which means, following the Bruggeman effective medium model, that the filling fraction of the $Si/SiO_2/SiO_x$ phases in the air is of the order of 45–50% (sample A) and 35–40% (sample B).

Transient THz conductivity spectra were measured at 20 K, 100 K, 200 K and 300 K in a usual setup for time-resolved THz spectroscopy [33] driven by a Ti:sapphire laser amplifier (Spitfire ACE, central wavelength 800 nm, 1 mJ pulse energy, 5 kHz repetition rate). A part of the laser beam was frequency doubled to 400 nm (3.10 eV) and defocused to generate photocarriers homogeneously across the sample (less than 25% of the pump beam power was transmitted through the 3 mm aperture placed in the sample position). The experiments were carefully performed as a function of the photocarrier density: the intensity of the pump beam was gradually decreased by neutral density filters down to ~1/400 of the maximum intensity (1.4×10^{15} photons cm^{-2}). The pump pulse delay in individual filters was calibrated using a film of CdS NCs [18] where the transient THz signal was sufficiently strong even at low photoexcitation densities and allowed us to set the zero pump–probe delay for each experiment.

4. Results and discussion

4.1. Theoretical analysis: experimentally accessible quantities

In this section, we develop a theoretical framework describing the THz signal in optically thick inhomogeneous samples. Similarly to [31], we consider here the limit of small photoinduced change of the THz field ($\Delta E_t \ll E_{\mathrm{inc}}$), where E_{inc} is the incident THz field. In the case of an exponential decrease of $\Delta\sigma(z)$ with z, which occurs when $\Delta\sigma(z)$ follows the spatial variation of the excitation density, the transient THz field ΔE_t transmitted through the sample reads:

$$\Delta E_t = -\frac{\mathrm{i}\Delta\sigma\,(z=0)}{\omega\varepsilon_0}\,\Xi\,E_{\mathrm{inc}},$$

where E_{inc} is the THz field incident on the sample and Ξ is the transfer function introduced in [32] and further discussed and specified for the most common experimental geometries in [31]. This is strictly true for homogeneous samples and this relation is also valid for percolated components where the linear equation between the microscopic and macroscopic conductivity holds [24]. In these cases the measured signal $\Delta E_t/E$ (where E is the transmitted signal through the sample without excitation) reads:

$$\frac{\Delta E_t}{E} = -\frac{\mathrm{i}\Delta\sigma\,(z=0)}{\omega\varepsilon_0}\,\frac{\Xi}{t_0}, \tag{10}$$

where t_0 is the complex transmittance of the sample in the ground state. It is easy to show that in the case of a thin film (i.e. optically thin with respect to the THz wavelength), in which the pump power is entirely absorbed, equation (10) reads in agreement with [27]

$$\Delta X_\sigma = -\frac{(n_1+n_2)}{z_0}\,\frac{1}{e\phi}\,\frac{\Delta E_t}{E} \tag{11}$$

which simply relates the normalized transient sheet conductivity to the measured transient THz spectra. Here z_0 is the vacuum wave impedance and n_1 and n_2 are THz refractive indices of the media surrounding the sample.

The macroscopic conductivity of the system with non-percolated component $\Delta\sigma_{NP}$ is related to the microscopic response by a nonlinear equation which means that it does not decrease exponentially with z for high pump fluences. Nevertheless, in [22] we argued that (11) is also valid for a general inhomogeneous *thin* film sample. However, a more rigorous justification of (11) and its generalization for thicker samples is lacking. Such a relation must be derived from the wave equation for the transient THz field (equation (2) in [31]):

$$\frac{\mathrm{d}^2\Delta E}{\mathrm{d}z^2} + k^2\Delta E = U\left(\omega, \omega_p; z\right) \tag{12}$$

where ΔE is the transient field inside the sample, k is its wave vector, and the appropriately defined right-hand side U accounts for the dependence of $\Delta\sigma$ on z.

We assume picosecond or slower dynamics of the photoexcited system which can then be analyzed within the so-called quasi-steady state approximation [31, 33]: the photoexcited state of the sample is assumed not to evolve during the duration of the probing THz pulse. This is equivalent to the condition that the frequency ω_p conjugated to the pump–probe delay τ_p is set to 0. The right-hand side U of (12) is given by equations (5) or (15) in [31]; for non-percolated photoconductive components we then obtain:

$$U(\omega; z) = -k_0^2 \frac{\Delta\sigma_{NP}(z)}{\mathrm{i}\omega\varepsilon_0} \times E_{inc} t_1 a \left[\exp(-\mathrm{i}kz) + r_2 \exp(\mathrm{i}k(z-2L))\right], \tag{13}$$

where $k_0 = \omega/c$ and L is the sample thickness. The parameter a describes multiple internal reflections of the THz beam inside the sample:

$$a = \left[1 - r_1 r_2 \exp(-2\mathrm{i}kL)\right]^{-1} \tag{14}$$

and r_1, r_2 are the internal reflection coefficients at the two sample surfaces and t_1 is the transmission coefficient of the input sample surface.

The wave equation is linear; therefore its partial solutions corresponding to individual additive source terms appearing at its right-hand side can be found separately and the final solution is then given by the sum of these partial solutions. In this sense, contributions from the percolated and non-percolated parts given by (3) can be treated separately and various components characterized by different conductivity mechanisms denoted by index j in section 2 can be also treated separately. The solution for the percolated part corresponds to that provided in [31]. In this paper we solve the equation for the non-percolated part. Note that all these solutions are summarized in the review [24].

We show in appendix B that the solution of the wave equation can be expressed in terms of the Gaussian hypergeometric function (B5 and B6). In the case of thin film samples the hypergeometric function terms simplify and tend to the logarithmic function given as the second right-hand side term in (9); the transient THz field then satisfies (11), which means that the transient sheet conductivity $\Delta\Sigma$ and normalized transient sheet conductivity ΔX_σ have a good physical sense for photoexcited thin films and that they are simply related to the raw experimental data by means of (11). For *thick* samples (several tens or hundreds of micrometers), the transient THz field is described by (B8) or (B9) and the presence of the hypergeometric function in this expression is related to the interferences of transient THz waves

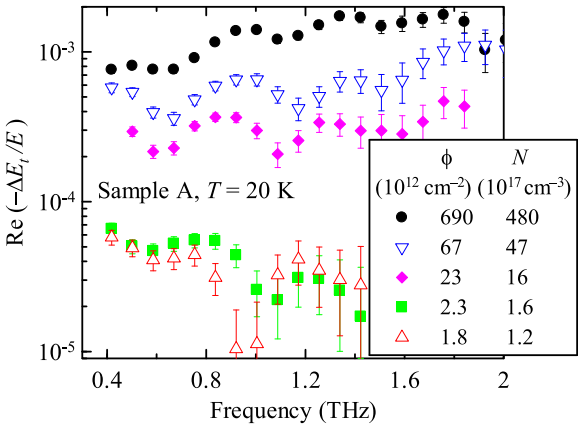

Figure 2. Real part of transient THz transmission spectra of sample A measured at 20 K with various pump fluences ϕ ($N_{\mathrm{NP}} \equiv N$ is the excitation density inside NCs).

generated backwards and forwards at different depths inside the sample, and of partial reflections at the excited/non-excited interface.

As suggested by the form of (B10), even in the most general case, the expression on the right-hand side of (11) has a convenient dimension and magnitude to characterize qualitatively the measured response. We will call this quantity normalized transient transmission ΔT_{norm}:

$$\Delta T_{\mathrm{norm}} = -\frac{(n_1 + n_2)}{z_0}\frac{1}{e\phi}\frac{\Delta E_t}{E}; \tag{15}$$

it is expressed in the units of mobility ($\mathrm{cm^2\,V^{-1}\,s^{-1}}$) and in the thin film limit $\Delta T_{\mathrm{norm}} = \Delta X_\sigma$.

4.2. Experimental results

The decay of the transient signal at various temperatures can be described by a single exponential curve with a characteristic lifetime of a few hundreds of picoseconds. This decay probably corresponds to the trapping of carriers in the states at nanocrystal boundaries, as the prevailing part of radiative recombination occurs on much longer time scales [7]. In this paper we do not focus on the carrier trapping and therefore we do not discuss these results in detail. We can simply state that the decay is much slower than the THz pulse length and we can calculate transient THz spectra by using the quasi-steady state approximation [33].

The transient THz spectra of Si NC samples were measured ~20 ps after photoexcitation. Figure 2 shows the frequency dependence of the real part of measured transient THz spectra at 20 K in the full range of excitation densities in sample A. Accumulating the transient THz spectra at the lowest excitation density (signal level below 10^{-4} with respect to the steady state transmission) took up to 17 h. The effective absorption coefficient α at 400 nm was measured to be 590 $\mathrm{cm^{-1}}$ and 500 $\mathrm{cm^{-1}}$ in sample A and B, respectively (penetration depths 17 and 20 μm, respectively). All measured transient spectra contain an interference pattern which is described by the general equation (B8) and taken into account in our fits. A first insight into the measured processes can be obtained by a qualitative analysis of the trends of the measured ΔT_{norm} from (15) which would be directly connected to the sheet conductivity in the thin film limit.

A qualitative inspection of the raw spectra in figure 2 clearly shows a change in the regime of the conductivity behaviour which accompanies the decrease of the photocarrier density: the

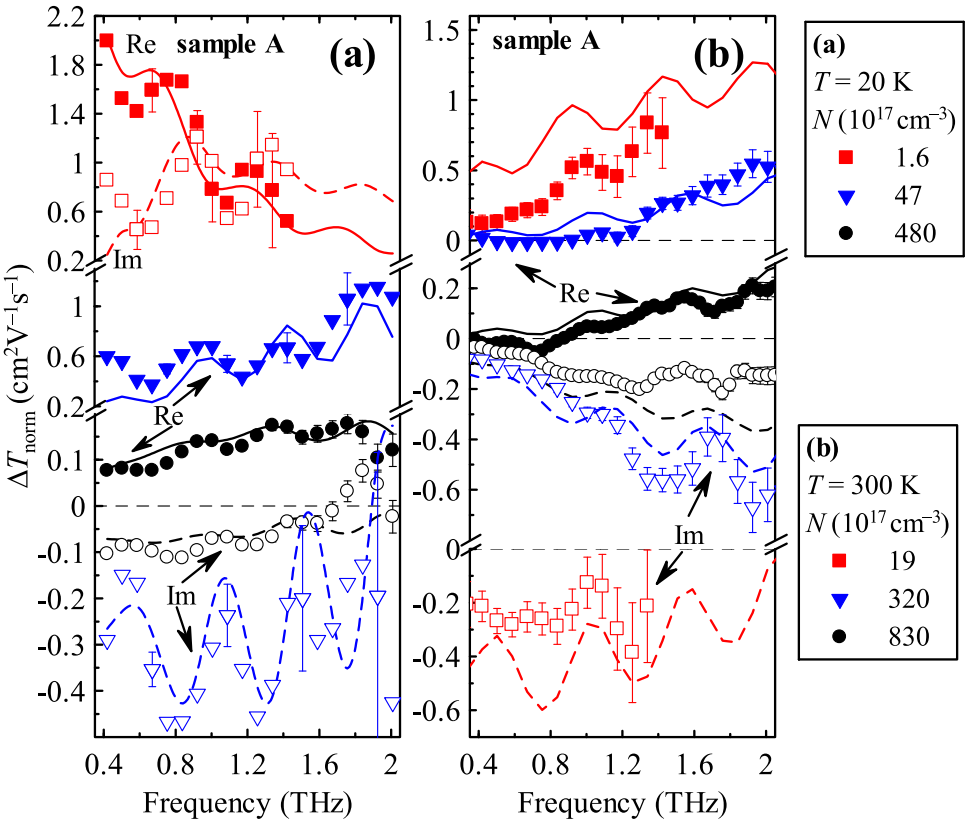

Figure 3. Examples of normalized transient THz transmission spectra in Si NC, sample A at 20 K (*a*) and 300 K (*b*). For each temperature, data obtained with high (black), medium (blue) and low (red) pump fluence are shown. Real part: closed symbols, imaginary part: open symbols; lines: fits. Sample thickness: 220 μm. Error bars (not shown for all points) correspond to the standard deviation of the average value obtained from data accumulations within a single experiment.

real part of $\Delta E_t/E$ increases with frequency for the highest pump power while its spectral decrease was recorded for the lowest pump powers. Selected normalized spectra ΔT_{norm} are shown as symbols in figures 3 and 4. This simple normalization of the raw signal defined by (15) reveals that the magnitude of the response per single absorbed photon increases with decreasing excitation density. Such a behavior indicates that a significant part of the THz photoconductivity originates in a non-percolated (NP) component of the sample which is strongly affected by depolarization fields.

4.3. Discussion

For the lowest excitation densities the depolarization fields are the weakest and the effective response of the NP component enters the linear regime. Under these experimental conditions the observed spectrum of ΔT_{norm} does not depend on the pump power upon its further decrease and it is most similar to the microscopic mobility of carriers. Indeed, the effective medium model does not transform the spectral shape any more as the denominator in (3) equals 1 in the THz range. Notably, in sample A at 20 K at the lowest excitation density (see figure 3(*a*)) the response shows characteristic features of the band-like transport of free carriers; if we disregard

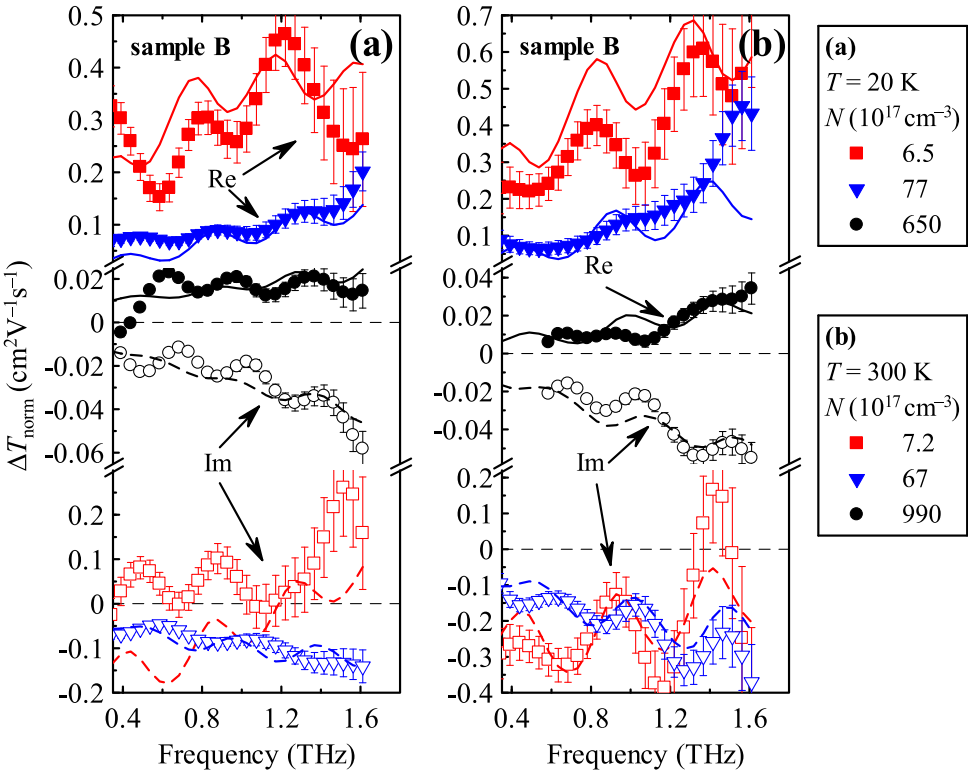

Figure 4. Examples of normalized transient THz transmission spectra in Si NC, sample B at 20 K (*a*) and 300 K (*b*). For each temperature, data obtained with high (black), medium (blue) and low (red) pump fluence are shown. Real part: closed symbols, imaginary part: open symbols; lines: fits. Sample thickness: 260 μm. Error bars correspond to the standard deviation of the average value obtained from data accumulations within a single experiment.

the interference effects, which will be discussed later, the real part of ΔT_{norm} decreases and its imaginary part is positive. Based on these observations, we apply a simple Drude model for the microscopic mobility to describe the observed spectra:

$$\xi_{\mathrm{D}}\,\mu_{\mathrm{D}}\,(\omega) \;=\; \frac{\xi_{\mathrm{D}}\,\mu_{D}}{1 + \mathrm{i}\omega\tau_{S}} \tag{16}$$

At each temperature, spectra of the normalized transient transmittance measured at different excitation densities were fitted together by excitation density-dependent analytic solution (B8) of the wave equation with the microscopic mobility spectrum described by the Drude model. Fitting parameters were s (filling fraction of the Si NC in the whole sample within the Maxwell–Garnett model), τ_S (scattering time) and the yield-mobility product $\xi_{\mathrm{D}}\mu_{\mathrm{D}}$. The shape factor K in (5) and (6) describing the Maxwell–Garnett effective medium approximation was set to 2 which represents particles with low anisotropy and aspect ratio close to 1. These fits revealed two remarkable features:

(1) The major part of the photoconductive response originates in an NP component that occupies only a very small volume fraction of the sample: s converged to values in the order of 2×10^{-4}. Later we will show that this Drude response is associated with the

electron motion in relatively large NCs. In figure 1(*a*) we plot a histogram showing the distribution of the nanoparticle diameters characteristic of our sample, obtained by analyzing images of AFM. It indicates the presence of large particles in the samples through the existence of a tail of the distribution towards larger sizes. The complimentary dynamic light scattering experiments (figure 1(*c*)) clearly demonstrate the existence of a broad tail of large particles. The photoluminescence of Si NC samples is proportional to the number of very small NCs. However, the THz conductivity does not scale with the *number* of NCs possessing a given size but rather with the total volume that the highly photoconductive NCs occupy in the sample. In fact, the THz mobility of carriers significantly decreases with decreasing size of NCs [21, 34]. In connection with these ideas we calculated the volume fraction (in the whole sample) of each bin from figure 1(*a*); the result is plotted in figure 1(*b*). We observe that, even if the experimental error is quite high for NCs larger than 25 nm, there is evidence that the total volume occupied by very large NCs will not be negligible.

(2) The single-component model fits the photoconductivity well for lower excitation densities (typically low and medium pump level in figures 3 and 4) but an additional term must be added to fit satisfactorily the data for all measured excitation densities within a single model. As this component comes out only for high pump fluences, it must be described by a term which does not suffer from substantial weakening owing to the depolarization fields. This condition is fulfilled in two cases: either the component is percolated, or it is non-percolated but characterized by such a low microscopic mobility that the macroscopic conductivity still scales linearly with the microscopic one [24]. However, the existence of percolation pathways in our samples is highly improbable; the volume fraction of Si NCs is rather low (2.5%), and moreover, the NCs are surrounded by an insulating oxide layer formed during the post-etching treatment.

As the nature of the carrier transport corresponding to the second component is unclear, we formally described it using the phenomenological Drude–Smith model [23]. We choose this model at this stage namely for practical reasons: to be able to perform a global fit of the data. Later on we will show Monte Carlo simulations describing the motion of the charges inside NCs and this will help us to understand the nature of this additional component. The Drude–Smith (DS) component reads as follows:

$$\xi_{\mathrm{DS}}\mu_{\mathrm{DS}}(\omega) = \frac{\xi_{\mathrm{DS}}\mu_{\mathrm{DS}}}{1 + \mathrm{i}\omega\tau_{\mathrm{DS}}}\left[1 + \frac{c_1}{1 + \mathrm{i}\omega\tau_{\mathrm{DS}}}\right] \tag{17}$$

τ_{DS} is the Drude–Smith relaxation time and c_1 is the Smith parameter which characterizes the probability of electron backscattering at the boundaries of nanoparticles [21]. The fitting was then performed using the prescription:

$$\Delta T_{\mathrm{norm}} = -\frac{(n_1 + n_2)}{z_0}\frac{1}{e\phi}\left[\left(\frac{\Delta E_t}{E}\right)_{\mathrm{DS}} + \left(\frac{\Delta E_t}{E}\right)_{\mathrm{D}}\right];$$

the transient signals $(\Delta E_t/E)_{\mathrm{DS}}$ and $(\Delta E_t/E)_{\mathrm{D}}$ are in principle both given by (B8). Assuming that the effect of depolarization fields is marginal for the Drude–Smith component, the first term simplifies to equations (21) and (22) in [31] (with $\omega_p = 0$) where we substitute for $\Delta\sigma = B_{\mathrm{DS}}\Delta\sigma_{\mathrm{mic,DS}}(\omega;0)$.

The absorption coefficient of Si NCs is significantly modified with respect to its bulk value only in the smallest NCs, which are not expected to contribute significantly to the THz conductivity spectra. Therefore we assume that local absorption coefficients in the D and DS components are the same: $\alpha_D = \alpha_{DS}$, and consequently the excitation densities are also equal: $N_D = N_{DS} \equiv N$.

The fitting parameters were s, c_1, τ_S, τ_{DS} and the products $\xi_D\mu_D$ and $B_{DS}\xi_{DS}\mu_{DS}$. Results of these complex fits are shown in lines in figures 3 and 4. The contribution of the Drude–Smith part to ΔT_{norm} is significant mostly at the highest excitation density when the conductivity peak of the Drude part is shifted to higher frequencies by the effect of depolarization fields. We clearly observe that, while the raw transmission ($\Delta E_t/E$) decreases with the photocarrier concentration (figure 2), the normalized transmission ΔT_{norm} exhibits a significant increase upon the decrease of N_{exc} and a qualitative change of the spectral shape. This change is marked namely for sample A at 20 K (figure 3). A global fit of the whole set of measurements (with variable N) was performed at each temperature; in these fits the least squares were weighted by the statistical error of the data (shown in figures 3 and 4). A very good match was achieved for all spectra (figures 3 and 4). The Drude component of our fits is shown in figure 5 for various carrier densities. We clearly observe a peak which shifts to high frequencies upon an increase of the carrier density. The peak in the real part is accompanied by a change of the sign in the imaginary part. This peak corresponds to a localized plasmon resonance and it is entirely due to the effect of the depolarization fields.

The oscillations in the spectra are due to the process of the transient signal build-up in a thick sample (dephasing between waves generated in backwards and forwards directions and their reflection on the excited/unexcited interface) which is described in detail in appendix B. The role of these effects is demonstrated in figure 6 where they are 'switched off' by neglecting the hypergeometric function in (B8). This is compared with the hypothetical signal obtained by neglecting the Fabry–Pérot reflections on the walls of the cuvette. It is clear that the oscillations in the spectra are caused dominantly by the former (i.e. transient) contribution while the interference due to the multiple reflections on the cuvette walls has only a negligible effect on the spectra.

In figures 3 and 4 the real and imaginary parts of the data evolve in a quite complex manner when the photoexcitation density is varied over more than two orders of magnitude. For example, we obtain an excellent agreement between the data and fit for sample A at 20 K. At high pump fluence (black plots) ΔT_{norm} (translating an 'effective conductivity per single absorbed photon') is rather low: the depolarization fields shift the conductivity peak to much higher frequency than the available spectral range as seen in figure 5(*a*). A decrease of the photoexcited carriers density (blue plot in figures 3(*a*) and 5(*a*)) first leads to an increase of both real and imaginary parts of ΔT_{norm} in absolute value; the imaginary part remains clearly negative and approaches zero slightly above 2 THz. By further lowering the photoexitation density the depolarization fields become weak and the conductivity peak passes through THz into the microwave range: in the red plot the band-like (Drude) transport is qualitatively apparent with the imaginary part positive and the real part showing a decrease with increasing frequency.

To illustrate this spectacular behavior even more clearly we calculated the expected normalized transient sheet conductivity of a thin sample (see figure 5(*b*)). In this plot we considered a sample with nominally the same properties as sample A (based on the fit results for sample A at 20 K) but with much smaller thickness of $L = 1\,\mu$m. For such a model sample the

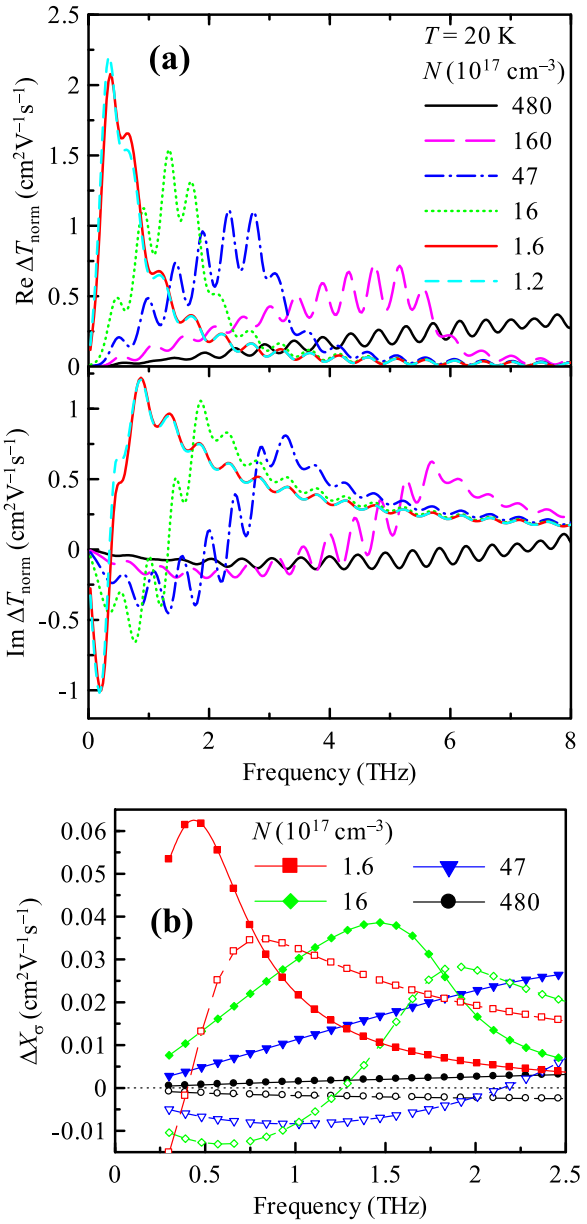

Figure 5. (*a*) Calculated Drude part of the normalized transient THz transmission spectra ΔT_{norm} in Si NC, sample A at 20 K over 8 THz for various carrier concentrations. (*b*) Normalized transient sheet conductivity of a model thin sample with nominally the same properties as the sample A at 20 K; sample thickness $L = 1\ \mu$m (in this case $\Delta X_\sigma = \Delta T_{\mathrm{norm}}$). Closed symbols: real part, open symbols: imaginary part. The Drude-like character of the response becomes apparent at low photoexcitation densities (red curve). The spectra in (*a*) and (*b*) show the spectral displacement of the localized plasmon peak towards higher frequency upon an increase of the carrier concentration. This phenomenon is in agreement with our experimental data; however, it is not so clearly visible in figure 3. Note also that the curves for the two lowest carrier densities in (*a*) are virtually the same.

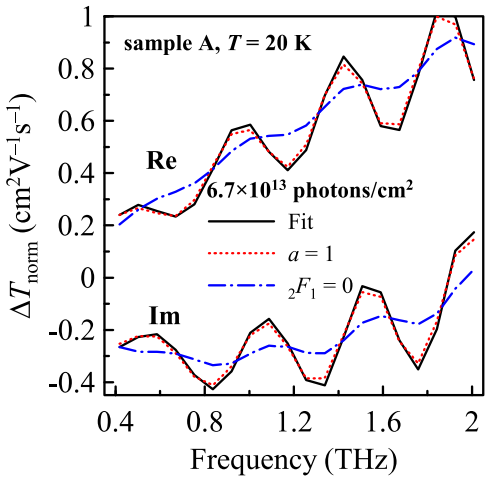

Figure 6. Spectra of ΔT_{norm} following (B8); black solid line: fit to the data (sample A, $T = 20$ K, moderate excitation density $N_{\mathrm{exc}} = 47 \times 10^{17}\,\mathrm{cm}^{-3}$), dotted red line: spectra with the same parameters but with $a = 1$ (equilibrium Fabry–Pérot internal reflections are neglected), dash-dotted blue line: spectra with the same parameters but terms where the hypergeometric function explicitly appears in (B8) are neglected (these terms describe interferences of various mutually dephased transient partial waves due to the generation process in the thick sample and due to reflections on the interface between the photoexcited and non-excited part of the sample).

thin film limit is valid ($\Delta T_{\mathrm{norm}} = \Delta X_\sigma$) and the response of the Drude part is described simply by (B16). The plot shows the basic behavior of the macroscopic conductivity characterized by the normalized transient sheet conductivity ΔX_σ without complicated interference effects which were unavoidably encoded into the experimental data. We clearly observe in figure 5(*b*) that, due to the build-up of the depolarization fields upon increasing the photocarrier density, the conductivity peak exhibits a large blue shift through the THz range and the THz response progressively weakens.

A similar but less pronounced trend is shown in figure 3(*b*) for $T = 300$ K. At higher temperature the Drude scattering time τ_{S} is significantly decreased due to additional scattering processes (namely scattering on longitudinal optical phonons); it follows that the THz photoconductive signal decreases and, under these conditions, we were not able to measure spectra at such low pump fluences to enter completely into the depolarization-free regime.

Sample B (figure 4) then shows a qualitatively similar behavior, however, we obtained a somewhat lower absolute signal for this sample and a somewhat shorter carrier scattering time.

Let us discuss the converged values of fitting parameters in both samples. The Smith coefficient c_1 was found, in general, to be close to -1 with the exception of sample B at 300 K where its value converged to -0.93. NP filling fraction s and the yield-mobility product $B_{\mathrm{DS}}\xi_{\mathrm{DS}}\mu_{\mathrm{DS}}$ are mostly temperature independent. These two parameters are three times larger in sample A than in sample B; $s \approx 2 \times 10^{-4}$ and $B_{\mathrm{DS}}\xi_{\mathrm{DS}}\mu_{\mathrm{DS}}$ is of the order of $0.15\,\mathrm{cm}^2\,\mathrm{V}^{-1}\,\mathrm{s}^{-1}$ for sample A. The scattering time τ_{S} and the relaxation time τ_{DS} follow similar temperature dependences both in sample A and in sample B, see figure 7. This suggests that τ_{DS} may be of similar origin, i.e. the DS component may arise from a confinement of the Drude-like motion inside smaller NCs. This process was described in [21], where the Drude–Smith relaxation time was shown to decrease progressively from the Drude scattering time value upon a decrease of

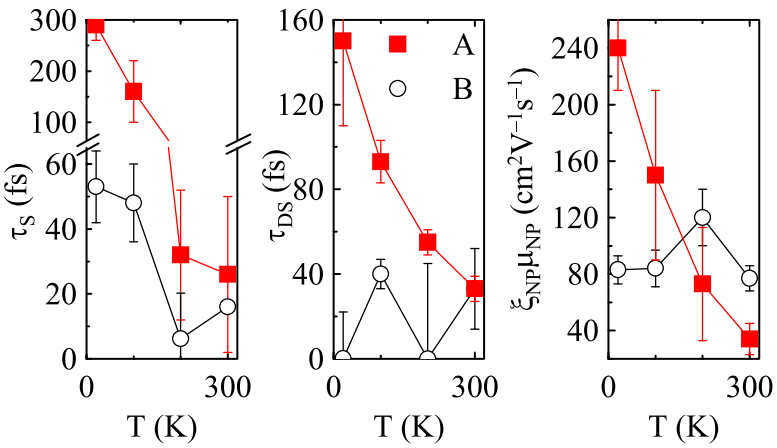

Figure 7. Temperature dependence of the fit parameters. NP component related to large NCs: Drude scattering time (τ_S) and yield-mobility product ($\xi_{NP}\mu_{NP}$); DS component related to small grains: Drude–Smith scattering time (τ_{DS}).

the NC size; exactly this behavior is observed in figure 7, τ_{DS} is comparable to or smaller than τ_S.

In order to quantify the origin of the Drude component, we carried out Monte Carlo calculations of the THz mobility spectrum [21] of isolated Si NCs with various sizes. We focus mainly on the sample A at low temperatures where the longest scattering time was observed as this situation provides the best opportunity for correlating the THz spectra with some characteristic size of nanoparticles. The results of simulations are shown in figure 8. Based on these results we can state that the Drude-like response is expected to entirely govern the microscopic mobility down to about 60 nm sized NCs. The shape of the mobility spectrum of such nanoparticles qualitatively corresponds to the observed spectrum (figure 3(*a*)). This implies that sample A must contain a small fraction of large (>60 nm) Si NCs which dominate the THz response at low to medium excitation densities.

Note, however, that the distribution of the NC size in our samples is very broad. The exact photoconductive response is then given by a sum of partial contributions over all NC sizes (weighted by their volume). It is not possible to infer such complete information from the experimental data. For this reason we approximate the real situation by two contributions (each describing a broader distribution of sizes) related to larger and smaller NCs. The amplitude of the signal due to smaller NCs is much lower than for the Drude component hence the role of depolarization fields should be weaker, in agreement with observations. We were unable to develop a more quantitative model, as the observed Drude–Smith component is rather weak; moreover, phenomena such as carrier–carrier scattering may already come into play for the highest excitation densities.

The temperature variation of the yield-mobility product of the Drude component in sample A correlates with the corresponding variation of the Drude scattering time. This is in agreement with the Drude-like picture of the motion where the amplitude of the mobility μ_D is proportional to the scattering time τ_S. From this we conclude that the quantum yield ξ_D is temperature independent. However, we deduce from the experimental data that its value reaches only about 10%; this indicates that a large fraction of photons creates carriers which are very rapidly trapped (<500 fs) or it is absorbed in surface-related defect states which do not interact with

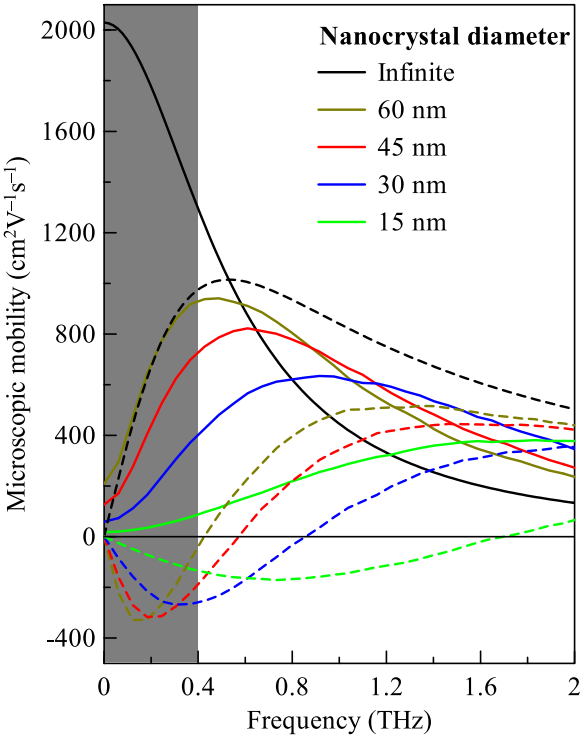

Figure 8. Spectra of microscopic mobility in Si NCs with various sizes at temperature 20 K (the Drude scattering time employed in the calculations was $\tau_S = 300$ fs) obtained by Monte Carlo simulations of carrier motion [21]. Solid lines: real part, dashed lines: imaginary part. The grayed part of the spectrum is not accessible experimentally.

THz radiation. Note that the large NCs probably have a spongy structure (due to etching) characterized by a large surface area which enhances the absorption near the surface. Photonic confinement effects may also be responsible for the decrease in the effective absorption [35]. The low yield may also partially stem from the distribution of sizes of NCs: smaller NCs within the given distribution exhibit lower amplitude of the electron mobility than in bulk; in turn, they contribute less to the $\xi_D \mu_D$ product.

Finally, it should be stressed that the observation of better photoconductive properties in the sample A (as compared with the sample B) is counter-intuitive and rather surprising (see figures 3 and 4). The additional treatment in the ultrasonic bath that sample A had been submitted to was expected to split large agglomerates (50–100 nm in diameter) of interconnected NCs and, accordingly, to break narrow conductive channels between them. The experiment did not confirm this expectation. Several hypotheses may be put forward to explain it:

(i) Under strong prolonged sonication, smaller aggregates of Si NCs approximately 20–30 nm in diameter are created, indeed (see figure 1), but being subsequently compressed in the measurement cuvette, the Si NCs cores may become connected to each other, giving rise to a higher microscopic conductivity.

(ii) For some of the NCs or aggregates their oxidized shell might be damaged and partially removed owing to sonication. This may favour the formation of Si NC aggregates with

good electrical connection among the crystalline cores; such aggregates then behave as effectively larger particles with higher microscopic conductivity.

(iii) An accidental presence of a few big 10-micrometer grains of bulk Si (as a reminder of the silicon wafer on which the native porous silicon was prepared) can overwhelm the contribution of Si NCs to the overall photoconductivity. In this respect, Si NCs samples with narrower size distribution and free of possible quasi-macroscopic inclusions will be needed for subsequent study.

On the one hand, this work demonstrates that THz spectroscopy is a tool capable of diagnosing very small amounts of large particles polluting truly NC samples. On the other hand, this finding shows that THz spectroscopic investigation of NC samples with small particle sizes requires samples free of larger signal-polluting particles.

Conclusion

Silicon nanocrystals fabricated by electrochemical etching were investigated by time-resolved THz spectroscopy. The spectroscopic technique provides data free of artifacts related to contacts; however, the local-field effects in NCs must be properly taken into account.

We solved the wave equation for THz pulse propagation in photoexcited inhomogeneous samples where depolarization fields can play a significant role. The proposed analysis retrieves information from the experimental data beyond the phenomenological level; it uncovers the photoconductive sample morphology and nanoscopic response of charge carriers in both thin and thick nanostructured samples.

The response of investigated nanocrystals is dominated by a Drude-like transport of charge carriers in a very small amount of large nanocrystals with characteristic size larger than $\sim$60 nm. The presence of a large-size tail is confirmed by dynamic light scattering measurements. For large excitation densities, depolarization fields screen this strong response, revealing a much weaker component that we described with the Drude–Smith term. Most likely, this component is related to the presence of NCs with a distribution of sizes in the range 10–30 nm. These nanocrystals are still too large to be responsible for the luminescence in the visible range.

The THz photoconductivity investigation turns out to be a complementary tool to photoluminescence spectroscopy for investigating ensembles of Si NCs with a size distribution. The photoluminescence intensity is proportional to the number of luminescent NCs, i.e., it provides information about tiny Si NCs a few nanometres in size. The THz technique essentially probes the sheet conductivity determined by the volume of structures with mobile carriers, usually dominated by large Si NCs or aggregates of electrically interconnected NCs. The optical spectra and electronic transport properties can thus be, in general, related to different effective NC size distributions.

Acknowledgment

We acknowledge the Czech Science Foundation which supports the presented research within projects 13-12386S and GPP204/12/P235. The work of VZ was supported by the grant 539612 of the Grant Agency of the Charles University and by the Specific University Research grant SVV-2013-267306.

Appendix A

Effective permittivity ε_{eff} of a multi-component system within Maxwell–Garnett approximation is given by

$$\frac{\varepsilon_{\text{eff}} - \varepsilon_{\text{m}}}{\varepsilon_{\text{eff}} + K\varepsilon_{\text{m}}} = \sum_l s_l \cdot \frac{\varepsilon_l - \varepsilon_{\text{m}}}{\varepsilon_l + K\varepsilon_{\text{m}}} \tag{A1}$$

where ε_l are the permittivities of the components, s_l are their volume fractions and ε_{m} is the permittivity of the matrix in which the components are dispersed. Considering that upon photoexcitation the permittivities change to

$$\varepsilon_l \to \varepsilon_l + \frac{\mathrm{i}\Delta\sigma_l}{\omega\varepsilon_0} \text{ and } \varepsilon_{\text{eff}} \to \varepsilon_{\text{eff}} + \frac{\mathrm{i}\Delta\sigma_{\text{eff}}}{\omega\varepsilon_0}, \tag{A2}$$

it is obvious that the effective transient conductivity $\Delta\sigma_{\text{eff}}$ must contain cross-terms ($\Delta\sigma_l\Delta\sigma_{l'}$) and, in the general case, equation (7) does not hold. If the volume fractions s_l are low and if the terms $(\varepsilon_l-\varepsilon_{\text{m}})/(\varepsilon_l+K\varepsilon_{\text{m}})$ are bounded (which comes true if the permittivities ε_l do not approach real negative values, i.e. far from underdamped localized-plasmon resonances), the cross-terms can be neglected and equation (7) becomes a good approximation.

Appendix B

To find the transient THz field transmitted through a photoexcited inhomogeneous sample with non-percolated conductive parts we need first to solve the differential equation (12) with the right-hand side (13):

$$\Delta E'' + k^2\Delta E = \left[X_F \exp(-\mathrm{i}kz) + X_B \exp(\mathrm{i}kz)\right] \times \frac{\exp(-\alpha z)}{1 + Y_0 \exp(-\alpha z)} \tag{B1}$$

with

$$X_F = -\frac{k_0^2\, B}{\mathrm{i}\omega\varepsilon_0}\Delta\sigma_0 E_{inc} t_1 a \tag{B2a}$$

$$X_B = -\frac{k_0^2\, B}{\mathrm{i}\omega\varepsilon_0}\Delta\sigma_0 E_{inc} t_1 a r_2 \exp(-2\mathrm{i}kL) \tag{B2b}$$

$$Y_0 = \frac{D\Delta\sigma_0}{\mathrm{i}\omega\varepsilon_0} \tag{B2c}$$

$$Y(z) = Y_0 \exp(-\alpha z) \tag{B2d}$$

where $\Delta\sigma_0$ is a microscopic conductivity at the surface of the sample in the non-percolated component, i.e. $\Delta\sigma_0 \equiv \Delta\sigma_{\text{mic,NP}}(\omega;0)$ in (8). The particular solution of the wave equation is found in terms of the logarithm which is at the origin of the non-percolated sheet conductivity term in (9):

$$\int \frac{\exp(-\alpha z)}{1 + Y_0 \exp(-\alpha z)} \mathrm{d}z = -\frac{\mathrm{Ln}\,[1 + Y(z)]}{\alpha Y_0} \tag{B3}$$

(where Ln stands for the principal value of the logarithm function) and of the Gaussian hypergeometric function ${}_2F_1$ (see e.g. [36]):

$$\int \frac{\exp[-(2\mathrm{i}k + \alpha) z]}{1 + Y \exp(-\alpha z)} \mathrm{d}z = -\frac{\exp[-(2\mathrm{i}k + \alpha) z]}{\alpha} \times \frac{{}_2F_1(1, 2\mathrm{i}k/\alpha + 1, 2\mathrm{i}k/\alpha + 2; -Y(z))}{2\mathrm{i}k/\alpha + 1}. \tag{B4}$$

For our specific arguments of the hypergeometric function we can simplify the notation by introducing a new function F in the following way:

$$F(\kappa, Y) = \frac{{}_2F_1(1, \kappa, 1 + \kappa; -Y)}{\kappa},$$

where $\kappa = 1 + 2\mathrm{i}k/\alpha$. The hypergeometric function can be expressed in a form of a series [36]; it then follows for the function F:

$$F(1 + 2\mathrm{i}k/\alpha, Y) = \frac{{}_2F_1}{(2\mathrm{i}k/\alpha + 1)} = \sum_{n=0}^{\infty} \frac{(-Y)^n}{2\mathrm{i}k/\alpha + (n + 1)} \tag{B5}$$

for $|Y(z)| < 1$ (see statement 15.1.1 in [36]), and

$$F(1 + 2\mathrm{i}k/\alpha, Y) = \frac{{}_2F_1}{(2\mathrm{i}k/\alpha + 1)} = \sum_{n=0}^{\infty} \frac{(-Y)^{-(n+1)}}{n - 2\mathrm{i}k/\alpha} + \frac{\Gamma(-2\mathrm{i}k/\alpha)\,\Gamma(2 + 2\mathrm{i}k/\alpha)}{2\mathrm{i}k/\alpha + 1} \times \exp\{-(2\mathrm{i}k/\alpha + 1)\,\mathrm{Ln}\,(-Y)\} \tag{B6}$$

for $|Y(z)| > 1$ (calculated from the statement 15.3.7 in [36]). One then obtains

$$\begin{aligned} \Delta E(z) = {} & \delta \exp(-\mathrm{i}kz) + \gamma \exp(\mathrm{i}kz) \\ & + \frac{X_F}{2\mathrm{i}k\alpha} \left\{ \frac{\mathrm{Ln}\,[1 + Y(z)]}{Y_0} - \exp(-\alpha z) F(1 + 2\mathrm{i}k/\alpha, Y) \right\} \exp(-\mathrm{i}kz) \\ & - \frac{X_B}{2\mathrm{i}k\alpha} \left\{ \frac{\mathrm{Ln}\,[1 + Y(z)]}{Y_0} - \exp(-\alpha z) F(1 - 2\mathrm{i}k/\alpha, Y) \right\} \exp(\mathrm{i}kz). \end{aligned} \tag{B7}$$

The magnetic field is obtained as follows: $-\mathrm{i}\mu_0\omega\,\Delta H = \mathrm{d}\Delta E/\mathrm{d}z$. Then the conditions of the continuity of the tangential transient electric and magnetic fields at the sample boundaries [32] (see also figure 9) lead to:

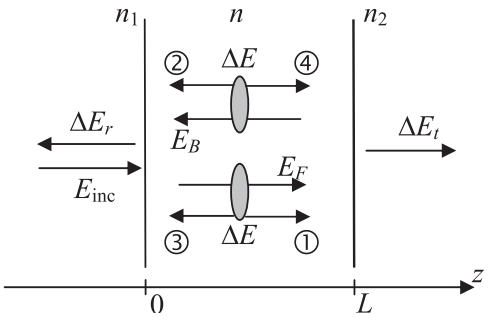

Figure 9. Explanation of the terms contributing to the transient THz signal. The physical meaning of the four terms in square brackets of (B9) is shown as secondary waves coming out of the forwards or backwards propagating source wave packet E (E_F and E_B, respectively). Equivalents of these four terms can be also easily identified in (B8).

$$\Delta E_t = -\mathrm{i}\frac{k_0 E_{inc} a^2 t_1 \exp(-\mathrm{i}kL)}{n+n_2}\frac{B}{D}\frac{Y_0}{\alpha}$$
$$\left[\left(1 + r_1 r_2 \exp(-2\mathrm{i}kL)\right)\frac{\mathrm{Ln}\left(1+Y_0\right) - \mathrm{Ln}\left(1+Y(L)\right)}{Y_0}\right.$$
$$+ r_1\left\{F\left(1+2\mathrm{i}k/\alpha, Y_0\right) - \exp(-2\mathrm{i}kL)\exp(-\alpha L)F\left(1+2\mathrm{i}k/\alpha, Y(L)\right)\right\}$$
$$\left. + r_2\left\{F\left(1-2\mathrm{i}k/\alpha, Y_0\right)\exp(-2\mathrm{i}kL) - \exp(-\alpha L)F\left(1-2\mathrm{i}k/\alpha, Y(L)\right)\right\}\right]. \quad \text{(B8)}$$

In order to simplify the resulting expressions we may further assume that the whole pump fluence is absorbed within the semiconductor sample, i.e., $\exp(-\alpha L) \to 0$, and the photocarrier concentration at the output face of the sample is negligible compared to that at the input face. However, we must keep in mind that we deal here with the non-percolated component where the macroscopic response saturates close to the input surface for a heavily excited sample following (3). In such a situation the transient signal coming from the region near the output face can be appreciable even if the carrier density is small there. Strictly speaking, we require a condition $|Y_0 \exp(-\alpha L)| < 0.1$ to be fulfilled (i.e. not too strong photoexcitation fluence) in order to be able to safely neglect the terms with $\exp(-\alpha L)$. We then obtain:

$$\Delta E_t = -\mathrm{i}\frac{k_0 E_{\text{inc}} a^2 t_1 \exp(-\mathrm{i}kL)}{n+n_2}\frac{B}{D}\frac{Y_0}{\alpha}$$
$$\left[\left(1 + r_1 r_2 \exp(-2\mathrm{i}kL)\right)\frac{Ln\left(1+Y_0\right)}{Y_0}\right.$$
$$+\left\{F\left(1+2\mathrm{i}k/\alpha, Y_0\right)r_1\right.$$
$$\left.\left. + F\left(1-2\mathrm{i}k/\alpha, Y_0\right)r_2\exp(-2\mathrm{i}kL)\right\}\right] \quad \text{(B9)}$$

where (B5) is substituted for $F(Y_0)$ if $|Y_0| < 1$ and (B6) is used if $|Y_0| > 1$. The physical meaning of the terms in (B9) is shown in figure 9. Note that the reference wave form E can be expressed as $E = t_1 t_2 a \exp(-\mathrm{i}kL) E_{\text{inc}}$ and, after this substitution, (B9) reads:

$$-\frac{n_1+n_2}{z_0}\frac{1}{e\phi}\frac{\Delta E_t}{E}=\frac{(n+n_1)(n+n_2)}{(2n)^2}\xi_{NP}\mu_{NP}\frac{\alpha_{NP}}{\alpha}B \times\left[\left(1+r_1r_2\exp(-2ikL)\right)\frac{\mathrm{Ln}\left(1+Y_0\right)}{Y_0} +\left\{F\left(1+2ik/\alpha,\,Y_0\right)r_1 + F\left(1-2ik/\alpha,\,Y_0\right)r_2\exp(-2ikL)\right\}\right]; \tag{B10}$$

in practice, the first fraction on the right hand side does not differ much from unity and it exactly cancels out with the terms issuing from the square brackets in the thin film limit.

1. In the limit of a small photoexcitation ($|Y_0|\to 0$) the depolarization fields are negligible and the non-percolated sample should behave linearly. Indeed, we obtain from (B9)

$$\Delta E_t \approx -E_{inc}\left(\frac{B\Delta\sigma_0}{i\omega\varepsilon_0}\right)\frac{k_0t_1}{n+n_2}\exp(-ikL)\,a^2\left[\frac{\left(1+r_1r_2\exp(-2ikL)\right)}{-i\alpha} + \frac{r_1}{2k-i\alpha}+\frac{r_2\exp(-2ikL)}{-2k-i\alpha}\right] \tag{B11}$$

which is exactly equivalent to equation (22) in [31] under appropriate conditions ($\omega_p=0$, $\exp[-\alpha L]=0$).

2. In the thin film limit ($\alpha\gg k$)

$$F\left(1+2ik/\alpha\to 1,\,Y_0\right)\to\frac{\mathrm{Ln}\left(1+Y_0\right)}{Y_0}, \tag{B12}$$

where we have used the identity [36]

$${}_2F_1(1,1,2;-X)=\frac{\mathrm{Ln}\,(1+X)}{X} \tag{B13}$$

and we obtain after some algebra

$$\Delta E_t\approx -i\omega\varepsilon_0E\frac{z_0}{n_1+n_2}\frac{B}{D\alpha}\mathrm{Ln}\left(1+Y_0\right), \tag{B14}$$

which can be rewritten as:

$$-\frac{(n_1+n_2)}{z_0}\frac{1}{e\varphi}\frac{\Delta E_t}{E}\approx B\frac{\mathrm{Ln}\left(1+\varphi\,\Delta\sigma_0\right)}{\varphi\,eN_{\mathrm{exc}}}=B\frac{\alpha_{NP}}{\alpha}\xi_{NP}\mu_{NP}\frac{\mathrm{Ln}\left(1+\varphi\,\Delta\sigma_0\right)}{\varphi\,\Delta\sigma_0}, \tag{B15}$$

an expression equivalent to (11), provided the principal value of the logarithm function is taken. Note also that if we cannot neglect the contribution coming from the region close to the output surface of the thin film, we obtain:

$$-\frac{(n_1+n_2)}{z_0}\frac{1}{e\varphi}\frac{\Delta E_t}{E}\approx B\frac{\mathrm{Ln}\left(1+\varphi\,\Delta\sigma_0\right)-\mathrm{Ln}\left(1+\varphi\,\Delta\sigma_0\exp(-\alpha L)\right)}{\varphi\,eN_{\mathrm{exc}}}. \tag{B16}$$

References

[1] Pavesi L and Turan R 2010 Silicon nanocrystals *Fundamentals, Synthesis and Applications* (Weinheim: Wiley-VCH)
[2] Khriachtchev L (ed) 2009 *Silicon Nanophotonics: Basic Principles, Present Status and Perspectives* (Singapore: Pan Stanford)
[3] Koshida N (ed) 2009 *Device Applications of Silicon Nanocrystals and Nanostructures* (New York: Springer)
[4] Belyakov V A, Burdov V A, Lockwood R and Meldrum A 2008 *Adv. Opt. Technol.* **2008** 279502
[5] Sa'ar A 2011 Photoluminescence in silicon nanostructures *Handbook of Nanophysics* vol 6 ed K D Sattler (Boca Raton, FL: CRC) pp 25–1
[6] Hartel A M, Gutsch S, Hiller D and Zacharias M 2013 *Phys. Rev.* B **87** 035428
[7] Trojánek F, Neudert K, Malý P, Dohnalová K and Pelant I 2006 *J. Appl. Phys.* **99** 116108
[8] Sykora M, Mangolini L, Schaller R D, Kortshagen U, Jurbergs D and Klimov V I 2008 *Phys. Rev. Lett.* **100** 067401
[9] Ondič L *et al* 2014 *Nanoscale* **6** 3837
[10] Žídek K, Pelant I, Trojánek F, Malý P, Gilliot P, Hönerlage B, Oberlé J, Šiller L, Little R and Horrocks B R 2011 *Phys. Rev.* B **84** 085321
[11] Wolkin M, Jorne J, Fauchet P M, Allan G and Delerue C 1999 *Phys. Rev. Lett.* **82** 197
[12] Luo J-W, Stradins P and Zunger A 2011 *Energy Environ. Sci.* **4** 2546
[13] Grätzel M 2003 *Nature* **414** 338
[14] Laforge J M, Cocker T L, Beaudry A L, Cui K, Tucker R T, Taschuk M T, Hegmann F A and Brett M J 2014 *Nanotechnology* **25** 035701
[15] Cooke D G, MacDonald A N, Hryciw A, Wang J, Li Q, Meldrum A and Hegmann F A 2006 *Phys. Rev.* B **73** 193311
[16] Cooke D G, MacDonald A N, Hryciw A, Meldrum A, Wang J, Li Q and Hegmann F A 2007 *J. Mater. Sci.: Mater. Electron.* **18** 447
[17] Titova L V, Cocker T L, Cooke D G, Wang X, Meldrum A and Hegmann F A 2011 *Phys. Rev.* B **83** 085403
[18] Mics Z, Němec H, Rychetský I, Kužel P, Formánek P, Malý P and Němec P 2011 *Phys. Rev.* B **83** 155326
[19] Jensen S A, Tielrooij K-J, Hendry E, Bonn M, Rychetský I and Němec H 2014 *J. Phys. Chem.* C **118** 1191
[20] Němec H, Kužel P and Sundström V 2010 *J. Photochem. Photobiol.* A **215** 123–39
[21] Němec H, Kužel P and Sundström V 2009 *Phys. Rev.* B **79** 115309
[22] Němec H, Zajac V, Rychetský I, Fattakhova-Rohlfing D, Mandlmeier B, Bein T, Mics Z and Kužel P 2013 *IEEE Trans. Terahertz Sci. Technol.* **3** 302–13
[23] Smith N V 2001 *Phys. Rev.* B **64** 155106
[24] Kužel P and Němec H 2014 *J. Phys. D: Appl. Phys.* **47** 374005
[25] Jeon T-I and Grischkowsky D 1997 *Phys. Rev. Lett.* **78** 1106
[26] Jeon T-I and Grischkowsky D 1998 *Appl. Phys. Lett.* **72** 2259
[27] Nienhuys H-K and Sundström V 2005 *Appl. Phys. Lett.* **87** 012101
[28] Tiwana P, Parkinson P, Johnston M B, Snaith H J and Herz L M 2010 *J. Phys. Chem.* C **114** 1365
[29] Dohnalová K, Ondič L, Kůsová K, Pelant I, Rehspringer J L and Mafouana R-R 2010 *J. Appl. Phys.* **107** 053102
[30] Dohnalová K, Pelant I, Kůsová K, Gilliot P, Galart M, Crégut O, Rehspringer J-L, Hönerlage B, Ostatnický T and Bakardjeva S 2008 *New J. Phys.* **10** 063014
[31] Kužel P, Kadlec F and Němec H 2007 *J. Chem. Phys.* **127** 024506
[32] Němec H, Kadlec F and Kužel P 2002 *J. Chem. Phys.* **117** 8454–66
[33] Fekete L, Kužel P, Němec H, Kadlec F, Dejneka A, Stuchlík J and Fejfar A 2009 *Phys. Rev.* B **79** 115306
[34] Wang F, Shan J, Islam M A, Herman I P, Bonn M and Heinz T F 2006 *Nat. Mater.* **5** 861

[35] Ponseca C S Jr, Němec H, Wallentin J, Anttu N, Beech J P, Iqbal A, Borgström M, Pistol M-E, Samuelson L and Yartsev A *Phys. Rev.* B at press

[36] Abramowitz M and Stegun I A 1972 *Handbook of Mathematical Functions with Formulas, Graphs, and Mathematical Tables 10th edn* (New York: Dover) pp 556–65